Article

Not peer-reviewed version

A Simple and Precise Procedure for a Complete Characterization of a Cone-Beam Computed Tomography System

Kun-Lung Shih , David, Shih-Chun Jin , Chia-Wei Wang , Jyh-Cheng Chen *

Posted Date: 27 January 2025

doi: 10.20944/preprints202501.1927.v1

Keywords: ellipse fitting; calibration; cone-beam computed tomography; precision alignment loop

Article

A Simple and Precise Procedure for a Complete Characterization of a Cone-Beam Computed Tomography System

Kun-Long Shih [1], David Shih-Chun Jin [1,2], Chia-Wei Wang [2] and Jyh-Cheng Chen [2,3,*]

[1] Department of Electro-Optical Engineering, National Taipei University of Technology, 106344 Taipei, Taiwan, ROC

[2] Department of Biomedical Imaging and Radiological Sciences, National Yang Ming Chiao Tung University, 112304 Taipei, Taiwan, ROC

[3] Department of Biomedical Imaging and Radiological Sciences, China Medical University, Taichung, Taiwan, ROC.

* Correspondence: jyhcheng@nycu.edu.tw

Abstract: In the calibration of cone-beam computed tomography (CBCT), two factors must be checked: the alignment of the imaging detector of the CBCT system and the effect of the slant sample platform. Earlier, we developed and validated a distinct procedure to accurately calibrate with precision any misalignment of the detector by using a cylindrical phantom with beads in a straight line, parallel to the axis of rotation of the CBCT system. Here, we generalize our earlier procedure to calibrate the CBCT system, then also detect and rectify a slight slant of the sample platform. We revise and validate our new procedure by calibrating the CBCT system, and it also determines the tilt angle between the central axis of phantom and the axis of rotation, when not 0°. The errors of misaligned angles for our new procedure are within ±0.03° which calibrates the CBCT system more precisely than our earlier work. To confirm that, we have performed a complete precise calibration of a dental CBCT system with the tilting sample platform. We also reconstruct a HA phantom in this CBCT system to analyze the quality of reconstruction. We present here a validated means to calibrate a CBCT system and rectify the effect of its tilting sample platform with good accuracy.

Keywords: ellipse fitting; calibration; cone-beam computed tomography; precision alignment loop

---

1. Introduction

Existing geometric calibrations rely on the decision of a parameters-set that accurately characterize the imaging system's geometry, which is setting the axis of rotation (AOR) normal to the sample platform. The well-known calibration phantoms containing steel beads set in some special pattern are used in most geometric calibration methods. The most types of extensively used phantom includes beads in circular [1–3], helical [4,5], a line [6–10], or other special arrangements [11,12].

Shih et al. [6] proposed and validated an analytic geometric scheme to calibrate, find and correct any misalignment in the imaging detector relative to the X-ray source. Here, we modify that scheme to include rectifying images taken with a tilt in the sample platform (or holder), thus calibrating the complete cone-beam computed tomography (CBCT) system including its tilt of sample platform. We validate this new scheme by using a helical-beads phantom and a line-beads phantom, allowing a tilt between the AOR and the central axis of the phantom (AOP). Sec. 2.1 will show the dental CBCT geometry and phantoms of calibration. Sec. 2.2 will show how the beads in the two chosen phantoms can have varied rotational radii. The fundamental theorem of an ideal CBCT system, where the beads in the phantoms may have varied rotating radii will be defined in Sec. 2.3. The precise relations between minor misalignment and perfect alignment will be delineated in Sec. 2.4–the relations that provide the necessary variables to depict the misalignment to constitute the foundation of the new

 doi:10.20944/preprints202501.1927.v1

precision alignment loop (PAL) generalized from our earlier version [6]. Sec. 3.1 will show the criterion for validating PAL's analytical simulations. Secs. 3.2 and 3.3 will validate the new PAL by detecting the misaligned parameter-set in the simulations for the helical-beads phantom (Sec. 3.2) and the line-beads phantom (Sec. 3.3) having a slightly tilted AOP with respect to the AOR. In our analytical simulations, we set the beads and the source of X-ray as points, and each bead was projected on a misaligned detector by stretching a line from the source to the bead to intersect the misaligned detector. Sec. 4 will present the calibrating results of a dental CBCT system using our new scheme.

2. Materials and Methods

2.1. The Dental CBCT Geometry

The dental CBCT system under study exposed in Figure 1a has a flat detector and an X-ray source on the opposite sides of a AOR mounted on a rotating gantry. The central ray from the X-ray focal point S, passes O on the AOR perpendicularly, and intersects the detector at the geometric center G, or simply "the center G". The three points, S, O, and G lie on the system's principal axis, the *z*-axis, originating from O pointing to S. The *y*-axis is the AOR. The *x*-axis with its origin at O follows the rule of right-hand screw. The distance between S and O is source-to-rotational-axis distance (SRD), and the distance between S and G is source-to-detector distance (SDD). The coordinate system that defines the detector's orientation is illustrated in Figure 1b.

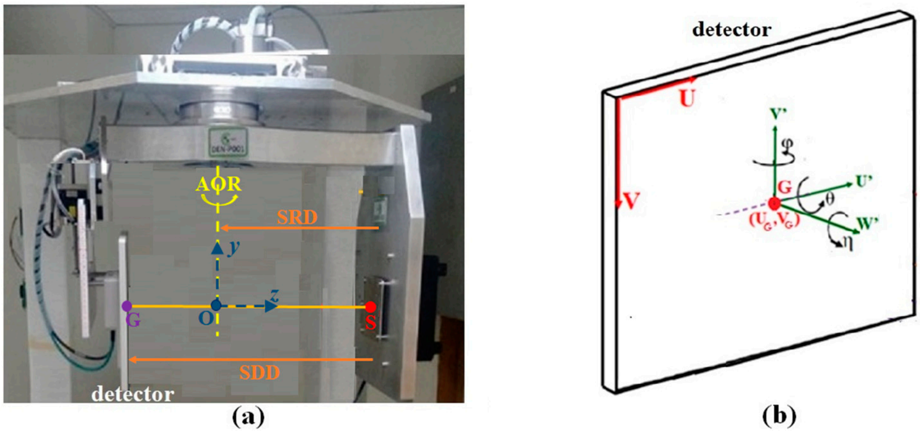

Figure 1. (a) The dental CBCT geometry. S stands for the X-ray point source, O is on the axis of rotation, and G is the detector's geometrical center. The x-axis points into the y-z plane which is not shown. (b) (θ, φ, η) are the three tilt angles of detector's local *U′*-*V′*-*W′* coordinate at G.

In an ideally aligned system, the *U′*-*V′*-*W′* coordinate, a local system, is a translation of the *x*-*y*-z coordinate, the global system, along *z*-axis to the detector. The position (U_i, V_j) of the (i, j)th pixel is given by *U*-*V* system, the body coordinate of detector, co-planar with the *U′*-*V′* system. If the system is not aligned, then the misalignment (θ, φ, η) can be characterized by a rotation of the axes at the center G: slant angle η about the *W′*-axis, skew angle φ about the *V′*-axis, and tilt angle θ about the *U′*-axis. In a misaligned system, as θ or φ is not zero, the *z*-axis is not overlapping with the *W′*-axis. The set (U_G, V_G, *SRD*, *SDD*, θ, φ, η) parameterizes the CBCT system. In an ideal aligned system, (θ, φ, η) = (0, 0, 0).

A misaligned system produces distorted images. Shih et al. [6] showed to find angles (θ, φ, η) accurately with precision can revive the fidelity of image. Our current approach varies from the previous works (cited in Sec. 1) by using PAL's iterative process that starts with a data set either from a simulation or an actual CT image to acquire the angles (θ, φ, η). The essence of PAL is exposed in Figure 2, but we modify it to include finding the tilt angle ζ between the AOP and the AOR in this study.

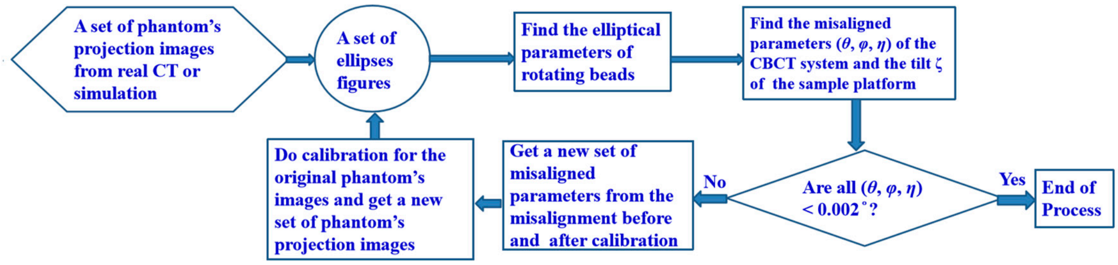

Figure 2. The PAL's flowchart.

We calibrate the CBCT system using a cylindrical phantom of helical-beads (Figure 3a), and a cylindrical phantom of line-beads (Figure 3c).The helical-beads phantom is a cylinder of 40-mm radius having eleven 2-mm diameter steel beads evenly separated by 36° in azimuth and 10 mm in height. The line-beads phantom is a cylinder of 40-mm radius having eleven 2-mm diameter steel beads by 10 mm even spacing on a line parallel to the AOP.

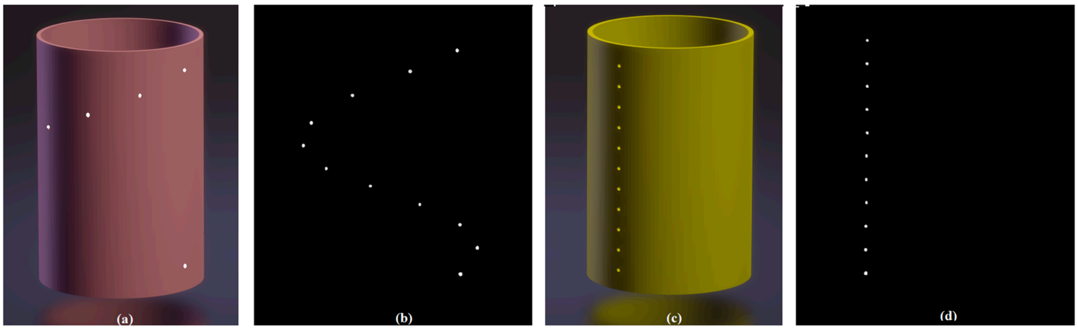

Figure 3. (a) The helical-beads phantom. (b) The inverted projection of helical-beads phantom after removing the background around the beads. (c) The line-beads phantom. (d) The inverted projection of line-beads phantom after removing the background around the beads.

We acquired a projection images-set of a calibration phantom, inverted the images, and then used a method of threshold segmentation to remove each projection's background around beads (Figure 3b,d), then applied the center-of-mass idea to the images to calculate out the exact beads' coordinates precisely.

2.2. Varied Rotational Radii of Beads in Phantoms

The beads on the two cylindrical phantoms shown in Figure 4 can have systematically varying radii of rotation under two conditions: 1) When the helical-beads phantom's AOP is parallel to the AOR, but displaced by a distance c in the x-z plane as exposed in Figure 4a; the beads' rotating radii of this phantom are within the range, r_P-c to r_P+c, where r_P is the radius of the phantom. 2) When there is a small tilt angle ζ between the line-beads phantom's AOP and the AOR, the beads' rotating radii of this phantom vary as exposed in Figure 3b. The tilt angle ζ can be deliberate by Eq. (1):

$$\sin\zeta = \frac{(r_N - r_1)}{(N\text{-}1)d} \tag{1}$$

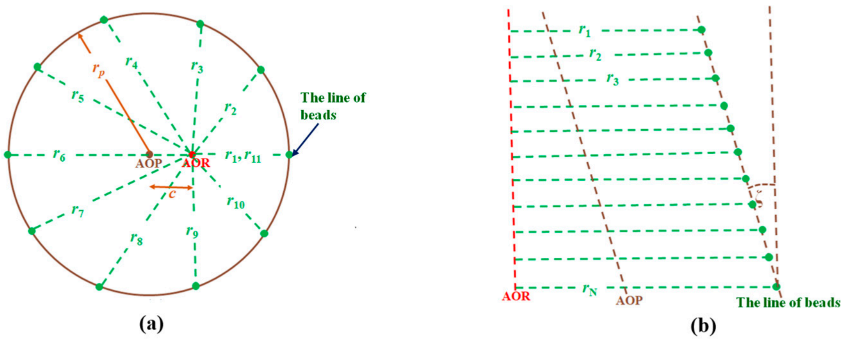

Figure 4. Two cases of varying radii of rotation. (a) When the helical-beads phantom's AOP parallels AOR, but displaced. (b) When the line-beads phantom's AOP has a tilt angle ζ from the AOR, where r_i is the i^{th} bead's rotational radius, d is two adjacent beads' vertical separation, and N is the number of beads.

where d is two adjacent beads' vertical separation, N is the number of beads, and r_1, r_2, r_3, …, and r_N are the respective beads' rotating radii of the line-beads phantom. Eq. (1) is also applied to the helical-beads phantom, since the first bead and the last bead are located on a line parallel to the AOP. For detecting the tilt angle accurately, it is important to setup the AOR, AOP, and the line of beads in the same plane.

The actual vertical separation d' must be modified according to Eq. (2):

$$d' = d \times \cos\zeta \tag{2}$$

2.3. The Ideal System

As shown in our previous work [6], the projections of the rotating beads on the detector are ellipses of different eccentricities. In an ideal detector, $\theta = \varphi = \eta = 0$. Figure 5 is a ray diagram showing points H, I, J, K, L, and M on the ideal detector (in yellow) as projections of the respective positions A, B, C, D, E, and F on a circular track traced out by a bead on the rotating phantom. The six critical projected points are sufficient to derive the equations to yield the necessary set of elliptical parameters: (U_L, V_L), the elliptical center; a and b, the semi-major and semi-minor axes; and η^*, the slant angle of the ellipse. In an ideal detector, $\eta^* = 0$.

As exposed in Figure 5a, two elliptical co-vertices J and M on the detector are the respective projected positions of C and F, therefore we have

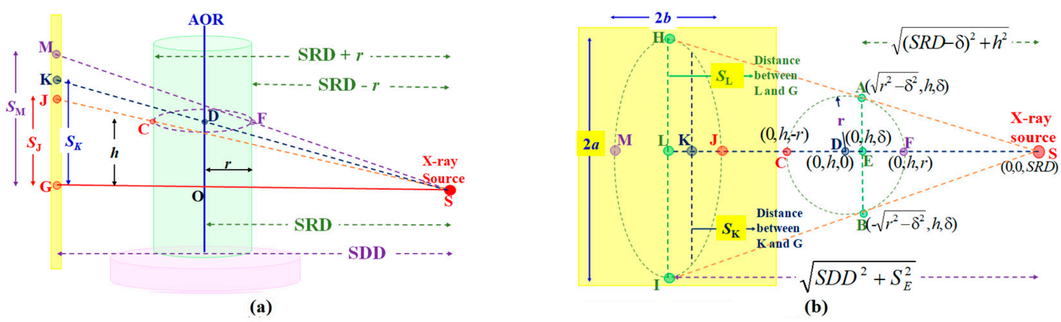

Figure 5. Two views of the projections on the detector (in yellow) of the critical points on a circular track of radius r of a bead rotating about the AOR for an ideal system. (a) J and M on the detector are the respective projected positions of C and F on the bead's circular track at $y = h$. K is the projection of D, the center of the circular track. (b) Critical points A and B on the bead's circular track in the x-z plane have their projections H and I, respectively. The six critical points' coordinates on the bead's circular track are exposed on the figure, where $\delta = r^2/SRD$.

Preprints.org (www.preprints.org) | NOT PEER-REVIEWED | Posted: 27 January 2025 doi:10.20944/preprints202501.1927.v1

$$S_J = h\frac{SDD}{SRD + r}; \qquad S_M = h\frac{SDD}{SRD - r} \tag{3}$$

where S_J and S_M are the distances from M and J (the co-vertices) to the center G (Figure 5a), respectively, r the bead's rotating radius, and h the distance from the rotating bead to the z-axis.

The system's magnification factor at D, the center of bead's circular track, M is related to the position of K, the projection of D on the detector:

$$M = \frac{S_K}{h} = \frac{SDD}{SRD}; \qquad S_K = \frac{SDD}{SRD}h = M \times h \tag{4}$$

where S_K is the distance from K to the center G, as exposed in Figure 5a.

The magnification factor M', at the critical positions of A, B, and E, is related to their respective projections at H, I, and L on the detector, as exposed in Figure 5b:

$$M' = \frac{SDD}{SRD - \delta} = \frac{S_L}{h} = \frac{a}{\sqrt{r^2 - \delta^2}} = \frac{SRD^2}{SRD^2 - r^2}\frac{SDD}{SRD} \tag{5}$$

where $\delta = r^2/SRD$, and S_L is the distance from the elliptical center L to the center G.

$$S_L = \frac{(S_M + S_J)}{2} = \left(\frac{SRD^2}{SRD^2 - r^2}\frac{SDD}{SRD}\right)h = M' \times h \tag{6}$$

The semi-major axis a and the rotating radius $r$are related according to Eq. (7):

$$a = r\frac{SDD}{\sqrt{SRD^2 - r^2}}; \qquad r = a\frac{SRD}{\sqrt{SDD^2 + a^2}} \tag{7}$$

Since the beads' rotating radii vary, those projected ellipses on the detector have different semi-major axes.

For the projected ellipse on the detector, the relations between 'b', the semi-minor axis, 'h', the rotating bead's height, 'r', this bead's rotating radius, and 'S_L', the distance between L, the center of the ellipse and the center G, are described by Eq. (8).

$$b = \frac{(S_M - S_J)}{2} = \left(\frac{SRD^2}{SRD^2 - r^2}\frac{SDD}{SRD}\frac{r}{SRD}\right)h = S_L\frac{r}{SRD}; \qquad S_L = \frac{b}{r}SRD \tag{8}$$

Eq. (8) gives S_L, the beads' projected elliptical centers as a function of b/r, semi-minor axis divides by respective bead's rotating radius, and $S_L = S_L(b/r)$. The S_L *vs.* b/r plot for the elliptical centers above and below the center G, yields V_G, since all the projected ellipses' centers constitute a vertical line, then we acquire the center G, (U_G, V_G), from which. After finding the center G, S_K can be calculated out by Eq. (4).

If a rotating bead is on the system's principal axis (z-axis), *i.e.*, $h = 0$, then on the detector, $b = 0$, and $S_L = 0$; and projection is a horizontal line of length $2a$ passing through the center G, a crucial point on the detector. Without a bead located at $h = 0$, however, we can still find G by considering the following. If we plot all the projected ellipses on the U-V plane, we see the ellipses flatten as the corresponding circular track's h approaches 0, as expected. This suggests that in a V_L *vs.* S_L plot, the ellipses will provide points to which two straight lines with opposite slopes can be fitted and they intersect at the V for G. This will be shown when we present the calibration results in Sec. 4.

As the rotating bead is closer to the z-axis, then $b \rightarrow 0$, on the detector. The elliptical parameters (U_L, V_L, a, b, η^*) will be acquired by the linear interpolation rather than fitting an ellipse.

In an ideal detector, the vertical projected distance, S_d, between two adjacent beads' rotating centers is the same, i.e.,

$$S_d = Md' \tag{9}$$

 doi:10.20944/preprints202501.1927.v1

2.4. The Misaligned System

We consider the condition as η, φ, and $\theta \le 10°$, then $\sin\eta \sim \eta$, $\sin\varphi \sim \varphi$, and $\sin\theta \sim \theta$, $\cos\eta \sim \cos\varphi \sim \cos\theta \sim 1$, and after neglecting the terms of second-order, then the simplified matrix of transformation T for a misaligned system is as:

$$T = \begin{bmatrix} 1 & 0 & 0 \\ 0 & \cos\theta & -\sin\theta \\ 0 & \sin\theta & \cos\theta \end{bmatrix} \begin{bmatrix} \cos\varphi & 0 & \sin\varphi \\ 0 & 1 & 0 \\ -\sin\varphi & 0 & \cos\varphi \end{bmatrix} \begin{bmatrix} \cos\eta & \sin\eta & 0 \\ -\sin\eta & \cos\eta & 0 \\ 0 & 0 & 1 \end{bmatrix} \approx \begin{bmatrix} 1 & \eta & \varphi \\ -\eta & 1 & -\theta \\ -\varphi & \theta & 1 \end{bmatrix} \tag{10}$$

The point (U_0, V_0, 0) on an aligned U'–V'–W' local system can be translated to (U_0+ $V_0\eta$, –$U_0\eta$ + V_0, –$U_0\varphi$ + $V_0\theta$) for a misaligned detector, with respect to the original coordinate system. (U_0 + $V_0\eta$, –$U_0\eta$ + V_0, –RDD –$U_0\varphi$ + $V_0\theta$) are their respective global Cartesian coordinates, where RDD = SDD – SRD. The small z coordinate's variation cause the varied magnification factor of four quadrants on a misaligned detector.

M_l and M_u are the respective magnification factors of the beads below and above z-axis:

$$M_l = M\left(1 - \frac{h_l \times \theta}{SRD}\right); \qquad M_u = M\left(1 - \frac{h_u \times \theta}{SRD}\right) \tag{11}$$

where h_l (h_l< 0) and h_u are the bead farthest below and farthest above z-axis, respectively. Therefore, Eq. (9), the average difference ΔS_d of the vertical projected separation between two adjacent beads' rotating centers below and above z-axis is:

$$\Delta S_d = (M_u - M_l) \times d' = \frac{M(h_u - h_l) \times d' \times \theta}{SRD} = \frac{S_d \times (\text{phantom's height}) \times \theta}{SRD} \tag{12}$$

$$\theta = \frac{\Delta S_d}{S_d} \times \frac{SRD}{(\text{phantom's height})} \tag{13}$$

where N is total bead number, $(N\text{-}1)*d' \le (h_u\text{–}h_l) \le (N\text{+}1)*d'$, and $(h_u\text{–}h_l) \approx$ phantom's height. The tilt angle θ of detector is acquired from Eq. (13). $N*d'$ is set as the phantom's height, since the calculated θ value and the setting value of the model are closer. Eq. (13) then acquires the tilt angle θ.

In a misaligned detector, the bead's positions A and B have distinct magnification factors caused by the tilt angle θ and skew angle φ. The positions H and I are their respective projection on the detector. Let M_A and M_B be the magnification factors for the bead's respective positions of A and B, then

$$M_A = \frac{[SDD + a\varphi - S_L\theta]}{SRD - \delta}; \qquad M_B = \frac{[SDD - a\varphi - S_L\theta]}{SRD - \delta} \tag{14}$$

In the case η = 0, $\theta \ne 0$, and $\varphi \ne 0$, then the two projected elliptical vertex points H and I on the detector are as follows:

$$(U_H, V_H) = (M_A\sqrt{r^2 - \delta^2}, M_A h); \quad (U_I, V_I) = (-M_B\sqrt{r^2 - \delta^2}, M_B h) \tag{15}$$

$$\eta^* \approx \tan\eta^* = \frac{(V_H - V_I)}{(U_H - U_I)} = \frac{(M_A - M_B)h}{(M_A + M_B)\sqrt{r^2 - \delta^2}} \approx \frac{h}{SRD - \delta}\varphi = \frac{S_L}{SDD}\varphi \tag{16}$$

A skew angle φ in a misaligned detector will cause a slant angle $\eta^* = \varphi \times S_L/SDD$ of this projected ellipse. As this rotating bead is on the system's principal axis, a horizontal line on the detector is traced out by the rotating bead, therefore η^* = 0. As $\eta \ne 0$, then η is the rotational angle about "W'-axis", which is normal to the plane of detector, therefore $\eta^* = \eta$ at the center G. The slant angle η^* in Eq. (16) is necessary to add "η" to the original η^* in each ellipse, then:

$$\eta^* \approx \eta + \frac{S_L}{SDD}\varphi \tag{17}$$

which shows η^* is linear to S_L and detector's skew angle φ. The slant angles η^* for all projected ellipses are plotted against 'S_L' of each respective bead to acquire the detector's skew angle φ from the plot's slope given by Eq. (17), and the slant angle η at the center G.

Since the first order angular approximation is used, there is larger difference between the calculated misalignment and the actual data values at larger misalignment ($>10°$). The PAL effectively reduces those differences.

The misaligned system is calibrated by the resulting angles (θ, φ, η) to acquire a new set of the near ideal detector's images. After that, we acquire the center G, (U_G, V_G), and M, the CBCT system's magnification factor, and SRD is re-acquired from Eq. (4), but we measure SDD from the CBCT system directly.

3. Validations

3.1. The Criterion for the Validation of Analytical Simulation

PAL's ability to detect misalignment and to restore alignment was tested on a detector of a dental CBCT having 2176×1792 pixels, with a pixel size of 0.139 mm in both dimensions. The SRD and SDD are respectively set at 430 mm and 620 mm, and SRD is re-acquired by Eq. (4). The inputs and results of these tests are presented in Secs. 3.2 and 3.3, and summarized in Tables 1 and 2, respectively. The input setting values of calibrated parameters are in bold shown in the row labeled "Model". In the row labeled "Found" are the misalignment found by the PAL's iterative process. PAL can accurately yield all the misalignment angles, SRD, and the geometric center (U_G, V_G) at once. Alignment is reached when (θ, φ, η) < 0.002° (3×10^{-4} rad) after calibration, as listed in the row labeled "Aligned". For this setup, all misaligned angles will be < 0.002° after calibration.

3.2. The Helical-Beads Phantom's AOP Has a Tilt Angle ζ from the AOR

First, the helical-beads phantom (Figure 3a) has its AOP set parallel to the AOR but offset by c = 10.0 mm (Figure 4a), after that, the AOP is tilted by a small angle ζ. Thus, the rotating radii of the beads are set from 30.0 mm to (50.0+100.0*sinζ) for all tests. The results of nine analytical simulations are exposed in Table 1. The errors in SRD are within 0.1 %, and that in (U_G, V_G) is within 0.5 pixels of the setting values. The errors of the misaligned angles (θ, φ, η) are within ±0.03° of the relevant setting values.

3.3. The Line-Beads Phantom's AOP Has a Tilt Angle ζ From the AOR

The line-beads phantom is exposed in Figure 3c, and its AOP has a small tilt angle ζ from the AOR. The rotating radii of the beads (Figure 4b) are set from 40.0 mm to (40.0 + 100.0*sinζ) mm for all simulations. The results of nine analytical simulations are exposed in Table 2. The errors in SRD are within 0.1%, and that in (U_G, V_G) is within 0.5 pixels of the setting values. The errors of the misaligned angles (θ, φ, η) are within ±0.03° of the relevant setting values.

From the simulated tests of Table 1 and Table 2, we find the two sets of results are almost the same with negligible difference. We conclude the calibrating results are independent of the choice of those two phantoms. The error of the tilt angle ζ between the AOP and the AOR is within ±0.004°of the setting values as $\zeta \leq 10°$. The error of angle ζ is increasing as ζ increasing, and this error is around 0.04%.

Table 1. The analytical simulations validation when the helical-beads phantom's AOP has a tilt angle ζ from the AOR.

Preprints.org (www.preprints.org) | NOT PEER-REVIEWED | Posted: 27 January 2025 doi:10.20944/preprints202501.1927.v1

Simulating Setups	U_G (pixel)	V_G (pixel)	SRD (mm)	θ (°)	φ(°)	η(°)	ζ(°)	Verification
	1000.000	**800.000**	**430.000**	**10.000**	**0.000**	**0.000**	**2.000**	**Model**
1	1000.000	798.519	421.356	9.999	0.000	0.000	2.699	Found
	1000.325	800.349	429.939	-0.001	0.000	0.000	2.000	Aligned
	1000.000	**900.000**	**430.000**	**0.000**	**10.000**	**0.000**	**3.000**	**Model**
2	991.696	899.983	429.980	0.000	10.000	0.001	3.049	Found
	999.700	900.014	430.016	0.000	0.000	0.000	3.000	Aligned
	1000.000	**1000.000**	**430.000**	**0.000**	**0.000**	**10.000**	**4.000**	**Model**
3	1019.396	996.336	436.595	0.000	0.000	10.000	4.061	Found
	1000.000	1000.000	429.995	0.000	0.000	0.000	4.000	Aligned
	1100.000	**800.000**	**430.000**	**1.000**	**1.000**	**1.000**	**5.000**	**Model**
4	1097.653	799.806	429.764	1.000	1.000	1.000	5.079	Found
	1099.995	800.041	429.987	0.000	0.000	0.000	5.000	Aligned
	1100.000	**900.000**	**430.000**	**2.000**	**2.000**	**2.000**	**6.000**	**Model**
5	1098.800	899.642	429.497	2.001	2.000	2.000	6.163	Found
	1099.999	900.000	429.974	0.000	0.000	0.000	6.000	Aligned
	1100.000	**1000.000**	**430.000**	**3.000**	**3.000**	**3.000**	**7.000**	**Model**
6	1103.442	999.502	429.186	3.004	3.000	3.000	7.254	Found
	1100.012	1000.112	429.953	0.000	0.000	0.000	6.999	Aligned
	1200.000	**800.000**	**430.000**	**4.000**	**4.000**	**4.000**	**8.000**	**Model**
7	1190.606	792.391	428.821	4.010	4.000	4.009	8.351	Found
	1199.638	800.312	429.913	0.000	0.001	-0.000	7.999	Aligned
	1200.000	**900.000**	**430.000**	**5.000**	**5.000**	**5.000**	**9.000**	**Model**
8	1196.989	890.534	428.389	5.019	5.001	5.012	9.455	Found
	1199.766	899.992	429.872	0.000	0.001	0.000	8.998	Aligned
	1200.000	**1000.000**	**430.000**	**6.000**	**6.000**	**6.000**	**10.000**	**Model**
9	1206.877	988.686	427.876	6.030	6.000	6.000	10.567	Found
	1199.983	999.978	429.815	0.000	0.001	-0.001	9.996	Aligned

Table 2. The analytical simulations validation when the line-beads phantom's AOP has a tilt angle ζ from the AOR.

Simulating Setups	U_G (pixel)	V_G (pixel)	SRD (mm)	θ (°)	φ(°)	η(°)	ζ(°)	Verification
1	**1000.000**	**800.000**	**430.000**	**10.000**	**0.000**	**0.000**	**2.000**	**Model**
	1000.000	798.519	421.272	9.999	0.000	0.000	2.930	Found

 doi:10.20944/preprints202501.1927.v1

	1000.325	800.349	429.938	0.000	0.000	0.000	2.000	Aligned
	1000.000	**900.000**	**430.000**	**0.000**	**10.000**	**0.000**	**3.000**	**Model**
2	990.802	899.980	429.982	0.000	10.000	0.001	3.050	Found
	999.700	900.014	430.015	0.000	0.000	0.000	3.000	Aligned
	1000.000	**1000.000**	**430.000**	**0.000**	**0.000**	**10.000**	**4.000**	**Model**
3	1019.396	1013.701	436.595	0.000	0.000	10.000	4.061	Found
	1000.000	1000.000	429.995	0.000	0.000	0.000	4.000	Aligned
	1100.000	**800.000**	**430.000**	**1.000**	**1.000**	**1.000**	**5.000**	**Model**
4	1097.499	799.805	429.748	1.000	1.000	1.000	5.102	Found
	1099.994	800.041	429.989	0.000	0.000	0.000	5.000	Aligned
	1100.000	**900.000**	**430.000**	**2.000**	**2.000**	**2.000**	**6.000**	**Model**
5	1098.425	899.639	429.457	2.001	2.000	2.000	6.209	Found
	1099.999	900.000	429.971	0.000	0.000	0.000	6.000	Aligned
	1100.000	**1000.000**	**430.000**	**3.000**	**3.000**	**3.000**	**7.000**	**Model**
6	1102.779	999.507	429.111	3.004	3.000	3.000	7.254	Found
	1100.008	1000.120	429.922	0.000	0.000	0.000	7.000	Aligned
	1200.000	**800.000**	**430.000**	**4.000**	**4.000**	**4.000**	**8.000**	**Model**
7	1189.585	792.419	428.700	4.009	4.000	4.008	8.442	Found
	1199.634	800.297	429.846	-0.001	0.001	0.000	7.997	Aligned
	1200.000	**900.000**	**430.000**	**5.000**	**5.000**	**5.000**	**9.000**	**Model**
8	1195.542	890.607	428.211	5.016	5.000	5.011	9.569	Found
	1199.790	899.993	429.704	0.000	0.000	0.000	8.996	Aligned
	1200.000	**1000.000**	**430.000**	**6.000**	**6.000**	**6.000**	**10.000**	**Model**
9	1204.934	988.834	427.627	6.025	5.999	6.014	10.703	Found
	1200.017	1000.059	429.825	0.000	0.001	0.000	9.996	Aligned

4. Results

4.1. Our Dental CT System

Having validated the efficacy of PAL, we use it calibrate our home-made dental CBCT system with the same geometry in Sec. 3. Ellipses on the detector are traced out by phantom's rotating beads, which form the PAL's input data, and the output of final result is the system to remove all misalignment after calibration, i.e., $(\theta, \varphi, \eta) \approx (0, 0, 0)$. With variances < 0.002° (3×10^{-5} rad).

4.2. Calibrating Our Dental CBCT System

Table 3 lists the elliptical center, (U_L, V_L), semi-axes a and b (in pixels), slant angle η^* for each ellipse, r is each bead's rotating radius, the value of $(b/r)\times$SRD is the projected distance of elliptical center to geometric center G, and V_K the projected distance of beads to the principal axis, all decided from the image CBCT by PAL handling directly from the calibration phantom, thus "before

Preprints.org (www.preprints.org) | NOT PEER-REVIEWED | Posted: 27 January 2025 doi:10.20944/preprints202501.1927.v1

calibration". In Table 3 and Table 4, each bead's rotating radius r, varies, as we expected when the AOP has a small tilt from the AOR.

Figure 6 is derived from Table 3. Figure 6a,b yield (U_G, V_G); Figure 6c and Eq. (13) yield θ = -0.277°; Figure 6d and Eq. (17) yield φ = 1.169° and η = -0.292°; thus (θ, φ, η) = (-0.277°, 1.169°, -0.292°) is the misalignment from the primary calculation before calibration. Through PAL, (θ, φ, η) = (-0.231°, 1.152°, -0.291°) is the misalignment from the final calculation. After calibration, we converted the misaligned parameters into "ideal aligned parameters", and final results are exposed in Table 4 and Figure 7. From Table 4, the tilt angle ζ between AOR and the AOP can be determined:

$\zeta = \sin^{-1}\{(51.821 - 53.646)/[(11 - 1) * 10)]\} = -1.046°$ (±0.001°).

After calibration, the geometric center G, (U_G, V_G) = (1028.706, 885.237) in pixels, and the CBCT magnification factor M is 1.4328 from Eq. (4), thence the SRD is 432.474 mm; Eq. (13) gives θ=(-5×10^{-4})°; Eq. (17) gives φ=(1×10^{-8})° and η=(-3×10^{-8})°. The misalignment of the detector are effectively reduced from (θ, φ, η) = (-0.231°, 1.152°, -0.291°) before calibration to (θ, φ, η) = ((-5×10^{-4})°, (1×10^{-8})°, (-3×10^{-8})°) after calibration by PAL, and the slant angles η^* of all ellipses are less than 4×10^{-5} rad (0.003°). The CBCT system reached within ±0.001° in all three directions of the ideal alignment after calibration.

Table 3. THE ELLIPTICAL PARAMETERS OF EACH BEAD FOR OUR DENTAL CBCT SYSTEM BEFORE CALIBRATION.

Bead No.	U_L(pixel)	V_L(pixel)	Semi-major axis (a)	Semi-minor axis (b)	η* (rad)	r(mm)	(b/r)*SRD(mm)	V_K(pixel)
1	1031.2101	160.3275	519.8593	79.3203	-0.00849	51.8307	97.3269	-731.5368
2	1031.0564	260.2956	451.6038	59.6192	-0.00801	45.0998	83.8444	-630.1795
3	1030.7361	359.1330	367.5386	40.9339	-0.00749	36.7676	70.1228	-526.6523
4	1030.4389	457.8673	294.6665	26.7232	-0.00704	29.5132	56.3831	-423.1621
5	1030.0572	555.1430	281.1494	19.6407	-0.00653	28.1648	42.7870	-321.1075
6	1029.5691	646.3118	333.6322	16.7880	-0.00611	33.3955	28.8167	-216.1962
7	1028.6118	756.4342	414.7303	11.2045	-0.00564	41.4503	15.2588	-114.1042
8	1026.8056	852.3691	489.3404	3.3211	-0.00515	48.8252	1.3589	-9.9114
9	1027.8958	962.8579	534.0376	8.8082	-0.00466	53.2246	12.4251	94.2877
10	1026.5521	1064.1786	537.0056	20.3251	-0.00422	53.5162	25.8672	195.0878
11	1025.8983	1169.7566	503.9358	30.3415	-0.00368	50.2634	39.3870	299.6775

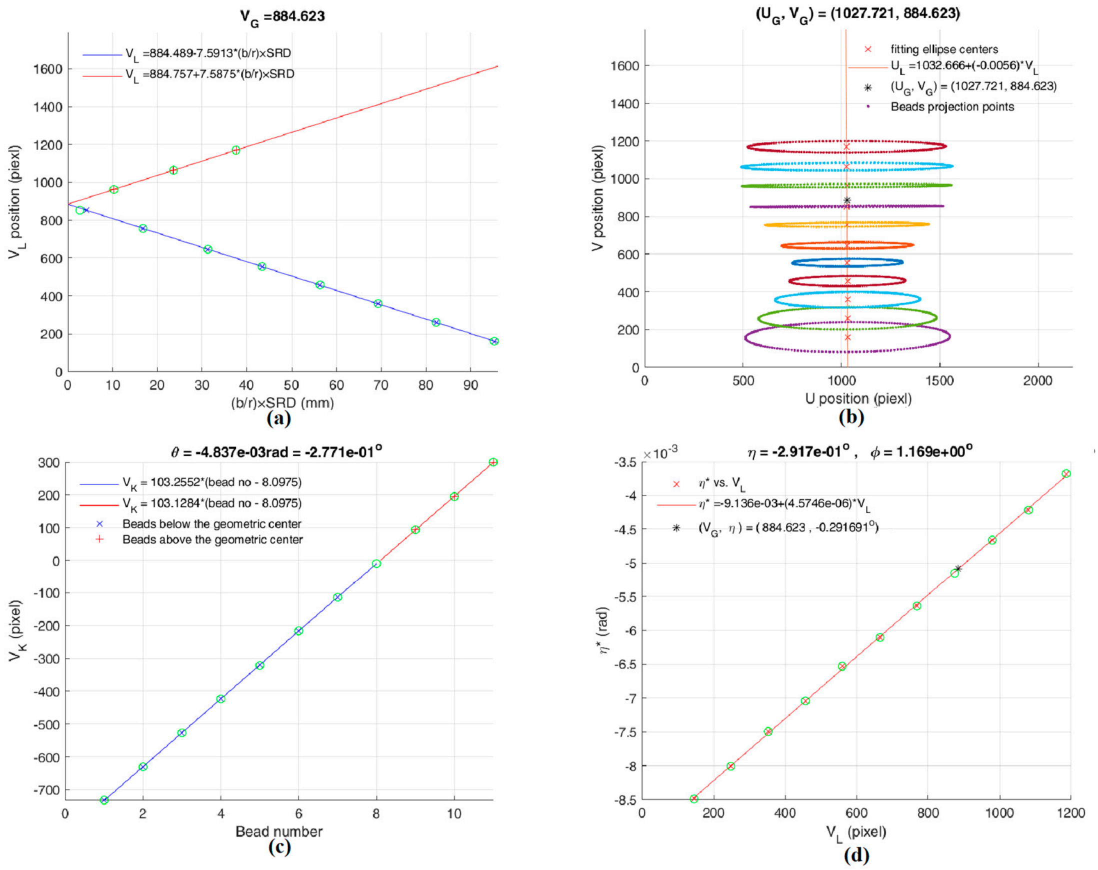

Figure 6. The primary calculated parameters of our dental CBCT system before calibration. (a) The ellipse center's position V_L *vs.* (*b*/*r*)*SRD. (b) The elliptical centers are exposed in *V*-*U* coordinates. (c) The projected rotational centers V_K vs. the bead number below and above *z*-axis. (d) The elliptical skew angle η* vs. V_L.

Table 4. THE ELLIPTICAL PARAMETERS OF EACH BEAD FOR OUR DENTAL CBCT SYSTEM AFTER CALIBRATION.

Bead No.	U_L(pixel)	V_L(pixel)	Semi-major axis (*a*)	Semi-minor axis (*b*)	η* (rad)	*r*(mm)	(*b*/*r*)**SRD*(mm)	V_K(pixel)
1	1028.6660	152.4467	539.6596	83.2825	0.00001	53.6460	97.2815	-731.0551
2	1028.7245	257.0081	466.3374	61.9410	0.00000	45.8087	83.8129	-629.8214
3	1028.5931	359.2661	377.5675	42.0892	0.00002	36.1071	70.1027	-526.3997
4	1028.5849	460.3167	301.1520	27.1958	-0.00001	27.6604	56.3723	-422.9981
5	1028.6759	558.8318	285.8904	19.7872	0.00002	26.0904	42.7827	-321.0099

Preprints.org (www.preprints.org) | NOT PEER-REVIEWED | Posted: 27 January 2025 doi:10.20944/preprints202501.1927.v1

6	1028.8164	650.2557	337.6639	16.7547	-0.00003	32.1808	28.8166	-216.1482
7	1028.7173	759.5510	417.3701	11.0565	-0.00003	41.5594	15.2604	-114.0851
8	1027.7668	853.7684	489.5930	3.2483	-0.00002	50.1466	1.3614	-9.8960
9	1029.6001	961.1178	531.7960	8.5112	0.00000	55.2690	12.4292	94.2989
10	1028.8055	1058.5057	532.0376	19.4388	-0.00002	55.6084	25.8771	195.1268
11	1028.5440	1158.9218	496.6324	28.7115	0.00004	51.8211	39.4054	299.7656

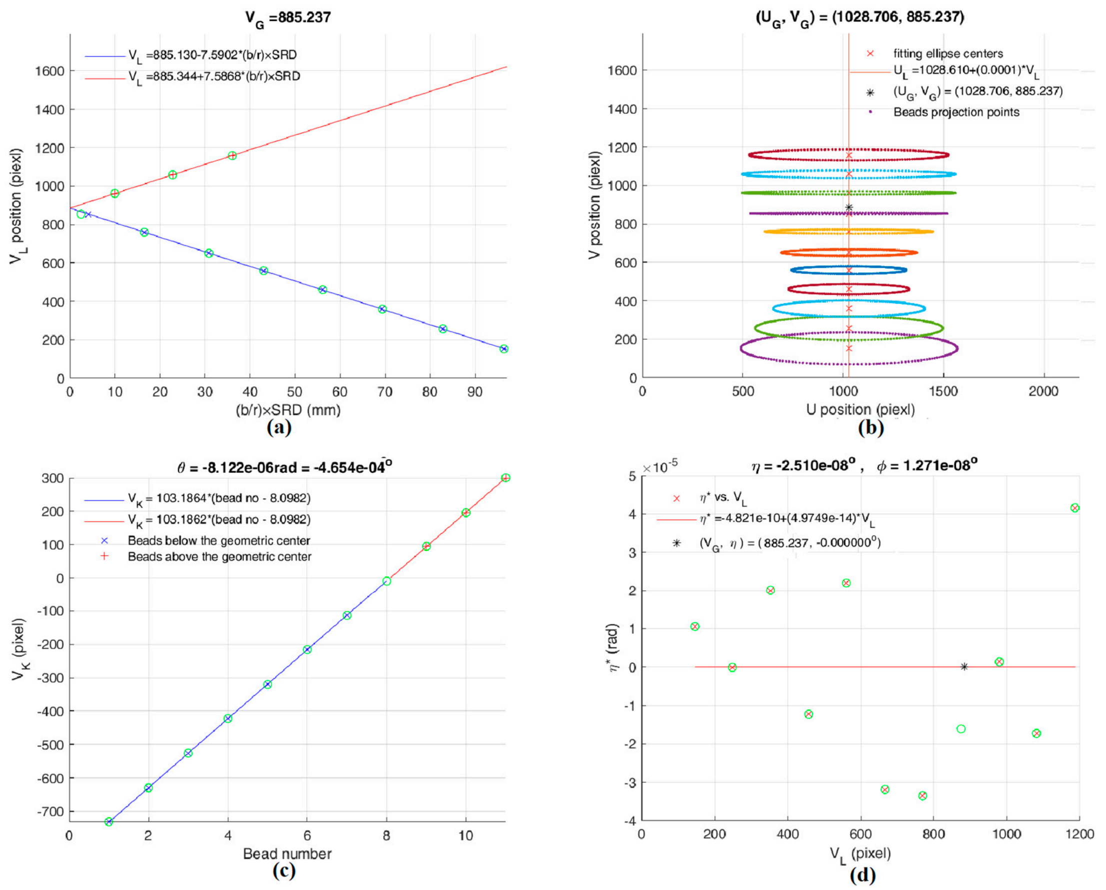

Figure 7. The final calculated parameters of our dental CBCT system after calibration. (a) The ellipse center's position V_L *vs.* (b/r)*SRD. (b) The elliptical centers are exposed in *V-U* coordinates. (c) The projected rotational centers V_K vs. the bead number below and above *z*-axis. (d) The elliptical skew angle η* vs. V_L.

4.3. Calibrating a Dental CBCT System with Analytical Simulation

An imitation CBCT system, similar to our dental CBCT, is calibrated to validate. The results of simulations is exposed in Table 5. The errors in SRD are within 0.01%, and that in (U_G, V_G) is within 0.02 pixels of the setting values. The errors of the misaligned angles (θ, φ, η) are within ±0.001° of the relevant setting values. The error of the tilt angle ζ between the AOP and the AOR is within ±0.001°of this setting value. The errors of measurement uncertainty in a real CBCT system are not included.

 doi:10.20944/preprints202501.1927.v1

Table 5. The validation of the analytical simulation for our dental CBCT system.

Simulating Setups	U_G (pixel)	V_G (pixel)	SRD (mm)	θ(°)	φ(°)	η(°)	ζ(°)	Verification
	1029.000	**885.000**	**432.000**	**-0.230**	**1.150**	**-0.290**	**-1.046**	**Model**
1	1028.193	884.699	432.038	-0.230	1.150	-0.290	-1.072	Found
	1028.984	884.997	432.000	-2×10^{-5}	1×10^{-4}	-1×10^{-4}	-1.046	Aligned

4.4. The Reconstructed Images of the HA Phantom

The HA phantom is designed to analyze the CT reconstruction quality. The reconstructed image of the HA phantom is exposed on Figure 8. There is blur circular edge for the reconstructed image without calibration. We do SNR and CNR analysis for image in CS region (slice number 365). Those two values are improved after calibration. The results are exposed in Table 6 and Table 7.

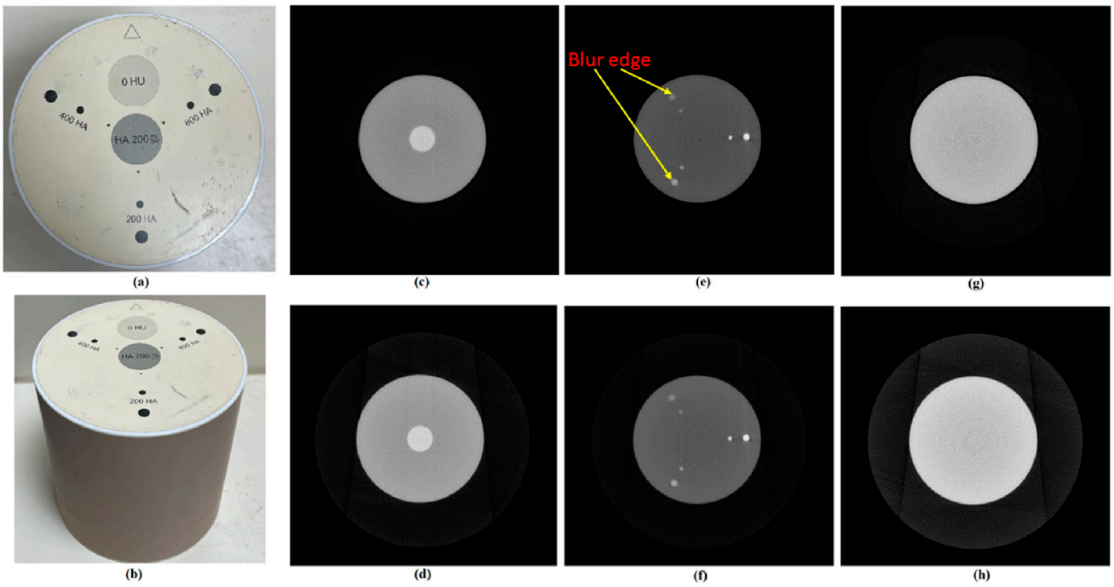

Figure 8. The HA phantom and its reconstructed images. (a) The top view of HA phantom. (b) The side view of HA phantom. (c) The reconstructed image of slice number 365 without calibration (CS region). (d) The reconstructed image of slice number 365 with calibration (CS region). (e) The reconstructed image of slice number 775 without calibration (HA region). (f) The reconstructed image of slice number 775 with calibration (HA region). (g) The reconstructed image of slice number 850 without calibration (water region). (h) The reconstructed image of slice number 850 with calibration (water region).

Table 6. The SNR and CNR for the reconstructed image without calibration of slice no. 365.

	Center	Up	Down	Left	Right
SNR	5.4567	4.4587	4.4811	4.4994	4.4583
CNR	/	1.3055	1.3055	1.2839	1.2846

Table 7. The SNR and CNR for the reconstructed image with calibration of slice no. 365.

	Center	Up	Down	Left	Right
SNR	7.0657	6.8115	6.7803	6.8228	6.8339
CNR	/	1.5661	1.5603	1.5449	1.5483

5. Discussions and Conclusions

Yang et al. [3] gave the errors of misaligned angles (θ, φ, η) within 0.04° and 0.1% error in SDD, but need precisely set beads' locations and configurations, and the AOP and the AOR overlap. Our previous work [6] required only the two axes be parallel but not overlap, and the beads' rotating radius > 10mm.

In this paper, we have revised and validated PAL, our precise calibrating algorithm, by using analytical simulations for the setting models and to calibrate a CBCT system by PAL with cylindrical phantoms of a helical-beads (Sec. 3.2) and a line-beads (Sec. 3.3), under three conditions: 1) the detector's misaligned angles (θ, φ, η) be each<10°, to fit the first-order approximation of the trigonometric functions in Eq. (10), the transformation matrix T; 2) all critical knowledge of misalignment comes from the parameters describing the ellipses projected on the detector by the beads with varied radii of rotation about the AOR; and 3) the AOP needs not be parallel to the AOR, but any small tilt angle ζ between the two axes can be determined.

We found our new procedure to: 1) calibrate the CBCT system more precisely than our previous work [6] in the errors of misaligned angles (θ, φ, η); 2) determine the tilt angle between the AOP and AOR, when not 0°; and 3) work equally well with different phantoms. We conclude that our generalized procedure presented above can give a complete, precise characterization of any CBCT system including a tilting sample platform.

6. Acknowledgments

This work was supported in part by the grand of MOST 109-2221-E-010-019-MY2, 110-2221-E-010-019-MY2, NSTC 112-2221-EA49-050-MY2 and 112-2811-E-A49A-002. We also thank K.C. Hsieh of the University of Arizona for helpful comments and suggestions.

References

1. Y. Cho, D. J. Moseley, J. H. Siewerdsen, and D. A. Jaffray, "Accurate technique for complete geometric calibration of cone-beam computed tomography systems," *Medical physics,* vol. 32, no. 4, pp. 968-983, 2005, doi: 10.1118/1.1869652..
2. J. C. Ford, D. Zheng, and J. F. Williamson, "Estimation of CT cone-beam geometry using a novel method insensitive to phantom fabrication inaccuracy: implications for isocenter localization accuracy," *Med Phys,* vol. 38, no. 6, pp. 2829-40, Jun 2011, doi: 10.1118/1.3589130.
3. H. Yang, K. Kang, and Y. Xing, "Geometry calibration method for a cone-beam CT system," *Med Phys,* vol. 44, no. 5, pp. 1692-1706, May 2017, doi: 10.1002/mp.12163..
4. S. Hoppe, F. Noo, F. Dennerlein, G. Lauritsch, and J. Hornegger, "Geometric calibration of the circle-plus-arc trajectory," *Phys Med Biol,* vol. 52, no. 23, pp. 6943-60, Dec 7 2007, doi: 10.1088/0031-9155/52/23/012.
5. M. Xu, C. Zhang, X. Liu, and D. Li, "Direct determination of cone-beam geometric parameters using the helical phantom," *Phys Med Biol,* vol. 59, no. 19, pp. 5667-90, Oct 7 2014, doi: 10.1088/0031-9155/59/19/5667.
6. K. L. Shih, D. S. Jin, Y. H. Wang, T. T. N. Tran, and J. C. Chen,"A simple and precise alignment calibration method for cone-beam computed tomography with the verifications," *Phys Med Biol,* Feb 15 2024, doi: 10.1088/1361-6560/ad29b8..
7. L. von Smekal, M. Kachelriess, E. Stepina, and W. A. Kalender, "Geometric misalignment and calibration in cone-beam tomography," *Med Phys,* vol. 31, no. 12, pp. 3242-66, Dec 2004, doi: 10.1118/1.1803792.
8. J. Xu and B. M. Tsui, "A graphical method for determining the in-plane rotation angle in geometric calibration of circular cone-beam CT systems," *IEEE Trans Med Imaging,* vol. 31, no. 3, pp. 825-33, Mar 2012, doi: 10.1109/TMI.2012.2183003.
9. J. Xu and B. M. Tsui, "An analytical geometric calibration method for circular cone-beam geometry," *IEEE Trans Med Imaging,* vol. 32, no. 9, pp. 1731-44, Sep 2013, doi: 10.1109/TMI.2013.2266638.
10. K. Yang, A. L. Kwan, D. F. Miller, and J. M. Boone, "A geometric calibration method for cone beam CT systems," *Med Phys,* vol. 33, no. 6, pp. 1695-706, Jun 2006, doi: 10.1118/1.2198187.

doi:10.20944/preprints202501.1927.v1

11. X. Li, Z. Da, and B. Liu, "A generic geometric calibration method for tomographic imaging systems with flat-panel detectors--a detailed implementation guide," *Med Phys,* vol. 37, no. 7, pp. 3844-54, Jul 2010, doi: 10.1118/1.3431996.
12. C. Mennessier, R. Clackdoyle, and F. Noo, "Direct determination of geometric alignment parameters for cone-beam scanners," *Phys Med Biol,* vol. 54, no. 6, pp. 1633-60, Mar 21 2009, doi: 10.1088/0031-9155/54/6/016..